ARCHIVES OF ELECTRICAL ENGINEERING VOL. 74(2), pp. 463–486 (2025)

DOI 10.24425/aee.2025.153909

Engineering practical thermal evaluation method of wrap-around liquid-cooled motor

QIANG HOU[1], YUEJUN AN[1]✉, MING LI[2], HUI AN[1],
YANJUN LU[3], NING SUN[1], CHANGLIN LIU[1]

[1] *School of Electrical Engineering, Shenyang University of Technology*
Shenyang 110870, China

[2] *School of Control Science and Engineering, Bohai University*
Jinzhou 121013, China

[3] *Shenyang KINGSEM Co., Ltd.*
Shenyang 110870, China

e-mail: ✉ *anyj_dq@sut.edu.cn*

(Received: 18.10.2024, revised: 11.05.2025)

Abstract: To meet the increasingly rigorous operational demands in motor applications, enhancing the torque output capacity has become a crucial area of focus for advancing industry growth. Given the limitations imposed by thermal constraints on a motor's torque output, this paper presents a wrap-around liquid-cooled thermal management system as an efficient solution, using a 40 kW permanent magnet synchronous motor (PMSM) as a case study. Additionally, to enable fast and accurate temperature distribution analysis of each motor component during the design phase, a magneto-thermal coupling model is developed based on a three-dimensional thermal network. This model incorporates both electromagnetic loss, node temperature, and thermal parameters while also accounting for the temperature-dependent characteristics of materials and thermal properties. The finite element analysis method and mock-up experiments verify the accuracy of the thermal evaluation model and cooling efficiency of the wrap-around liquid-cooled motor. The proposal of the wrap-around liquid-cooled scheme further improves the thermal management efficiency of the motor, with a 44.5% increase compared to the indirect casing cooling scheme. The establishment of a coupled model not only improves the accuracy of analysis, but also significantly reduces the cycle of thermal evaluation, which has important guiding significance for the design and optimization of motors in engineering practice.

Key words: engineering practice, magneto-thermal coupling, mock-up experiment, temperature characteristics, three-dimensional thermal network, wrap-around liquid-cooled

---

1. Introduction

In certain specialized applications, permanent magnet synchronous motors (PMSMs) must exhibit high overload capacity, reliability, and lightweight design. However, the elevated power density in these motors leads to significant stator winding temperature rises due to high electrical current, which in turn can result in the irreversible demagnetization of the permanent magnets. Consequently, thermal limitations have become a key constraint in further enhancing the overload capacity of PMSMs [1].

Facing the challenge of motor performance being limited by temperature rise, scholars globally have employed high-efficiency cooling systems to mitigate this issue. The most common motor cooling systems are air-cooled and liquid-cooled. In reference [2], air cooling is applied, but its low efficiency restricts the motor's torque output. Reference [3] adopts casing cooling for thermal management, yet it presents high thermal resistance, with the hottest point occurring at the winding end. Reference [4] adopts an oil immersed direct oil cooling heat dissipation system, which immerses the key components of the motor in cooling oil. The cooling liquid directly contacts the heat sources such as windings, stator, and rotor inside the motor cavity, greatly reducing the thermal resistance of high heating components of the motor and solving the problem of difficult heat dissipation at the end. However, the high viscosity of oil can cause strong fluid friction during the rotation of the rotor. Moreover, the rotation of the rotor can cause turbulence and vortex effects in the cooling oil, especially in open oil chamber designs, which can result in certain stirring losses and increase energy loss during rotor rotation. At the same time, it is necessary to strictly filter the oil medium to avoid impurities in the oil damaging the motor insulation layer, and the sealing requirements for the motor are also high, which increases the design cost of the cooling system.

For evaluating the thermal performance of motors, commonly used methods include the Lumped Parameter Thermal Network (LPTN), Finite Element Analysis (FEA), and Computational Fluid Dynamics (CFD). FEA, while highly accurate, requires significant time for both modeling and computation. Additionally, it often employs experience-based convection boundary algorithms on solid surfaces, leading to varying accuracy [5]. CFD provides precise temperature assessments for each motor component, but its high computational time and cost make it impractical for quick thermal evaluation and optimization in engineering applications [6]. LTPN, through an equivalent network composed of thermal resistance and heat capacity, can quickly evaluate temperature distribution and heat transfer processes with low computational time cost [7]. The commonly used methods for electromagnetic analysis based on motors include analytical method, lumped parameter magnetic network method, and finite element analysis method. The finite element method can describe complex geometric structures and nonlinear characteristics in detail, but it also has the disadvantages of high computational resource requirements and long solution time [8]. Although the analytical method has the shortest calculation cycle, it cannot consider characteristics such as magnetic leakage, iron core saturation, and asymmetry, resulting in lower calculation accuracy [9]. The lumped parameter magnetic network method has fewer meshing elements compared to the finite element method, and does not require repeated meshing. At the same time, it can consider practical problems such as leakage flux, nonlinear saturation of ferromagnetic materials, and cogging effects, while balancing the accuracy and solving speed of motor performance calculations [10]. So, modeling separately through magnetic and thermal networks can significantly reduce computational complexity. It is worth mentioning that the magnetic network and thermal network can be flexibly adjusted according to the actual structure of different motors, such as slot type, iron core shape, cooling system layout, etc., and have good scalability [11]. More importantly, magnetic networks and thermal networks can be designed at different levels. Magnetic networks can capture the complex geometric characteristics and material nonlinearity of motors, while thermal networks can capture the distribution of heat sources and thermal conduction paths. The two can be coupled with each other through clear physical quantities such as power loss and heat source distribution, forming a new mechanism for hierarchical solving. In addition, network models provide efficient performance evaluation tools in multi-objective optimization design (balancing power density, efficiency, and cooling performance) of motor [11]. Therefore, using magnetic and thermal networks to separately calculate electromagnetic and thermal problems fills the gap between efficient design and rapid analysis, and provides a compromise solution that combines engineering practicality and theoretical accuracy.

Currently, temperature rise in Permanent Magnet Synchronous Motors (PMSMs) is typically determined through unidirectional coupling analysis. However, this approach overlooks the thermal properties of motor materials, making it insufficient to precisely represent the motor's actual working conditions. As a result, performing bidirectional coupling analysis on the magneto-thermal model of the motor becomes essential. Studies like those in references [12–15] employ FEA and LPTN methods to solve the motor's electromagnetic and thermal fields. These studies establish a bidirectional coupling model combining FEA and LPTN for iterative computation, which is time-efficient. Nevertheless, this model does not account for circumferential heat transfer in the temperature field, resulting in lower calculation accuracy. In references [16–19], the FEA method is utilized to independently examine the electromagnetic and thermal fields, thereby improving the precision of iterative computations. However, the FEA-FEA coupling model does not account for the temperature-dependent variations in thermal conductivity and heat dissipation coefficient. References [20–22] develop an FEA-CFD model for PMSM, enhancing the precision of motor temperature rise predictions. However, its implementation in practical engineering is limited by the high computational time and resource requirements.

In the multi physics bidirectional coupling calculation of permanent magnet synchronous motors, traditional calculation models usually assume constant material parameters, but this simplification can no longer meet the requirements of refined design, because the significant influence of temperature on electromagnetic material parameters and thermal parameters cannot be ignored. The core of this problem lies in the fact that the interactions in multiple physical fields are not static, but dynamically coupled. Specifically, the characteristics of electromagnetic materials (such as conductivity and magnetic properties of permanent magnets) and thermal properties (such as thermal conductivity and heat dissipation coefficient) exhibit nonlinear patterns with temperature changes, which directly affect the prediction and design optimization of electromagnetic and cooling performance of motors. Therefore, in order to quickly and accurately evaluate the cooling performance of permanent magnet synchronous motors, this paper establishes a multi physics bidirectional coupling calculation model of magnetic network and thermal network. In order to accurately describe this coupling effect, a dynamic three-dimensional mapping relationship of electromagnetic characteristics temperature thermal characteristics is constructed. Under the framework of multi physics bidirectional coupling, the temperature dependence of electromagnetic materials and thermal parameters is considered simultaneously. On the one hand, the dynamic behavior of magnetic networks requires dynamic coupling between electromagnetic field equations and temperature dependent functions of materials. On the other hand, the description of thermal networks requires the introduction of nonlinear heat transfer equations for modeling.

In an effort to further minimize the thermal resistance between the cooling medium and the heat source, this study introduces an innovative thermal management approach—direct liquid cooling utilizing wrap-around windings. The unique structure of this direct cooling system necessitates extensive and intricate physical modeling during the initial phase when employing numerical analysis to assess its heat dissipation capabilities. Additionally, the computation of magnetic and thermal parameters requires considerable computer resources, prolonging the thermal evaluation process. To enhance the accuracy and efficiency of predicting the temperature distribution across various components of a wrap-around liquid-cooled motor in engineering applications, a thermal evaluation model is developed. This model couples electromagnetic loss, node temperature, and thermal parameters based on a three-dimensional thermal network. The model's reliability and precision are confirmed through both finite element analysis and experimental mock-ups, forming the key contribution of this study. Subsequently, the established coupling model is employed to assess the heat dissipation potential of the wrap-around liquid-cooled system, providing valuable guidance for motor design and optimization.

2. Proposal of wrap-around liquid-cooled scheme

This study focuses on a 40 kW Permanent Magnet Synchronous Motor (PMSM) featuring a surface-mounted permanent magnet rotor and concentrated windings within the stator slots. Figure 1 illustrates the topology of the proposed concept verification PMSM motor. The key electrical performance characteristics and dimensional parameters are detailed in Table 1.

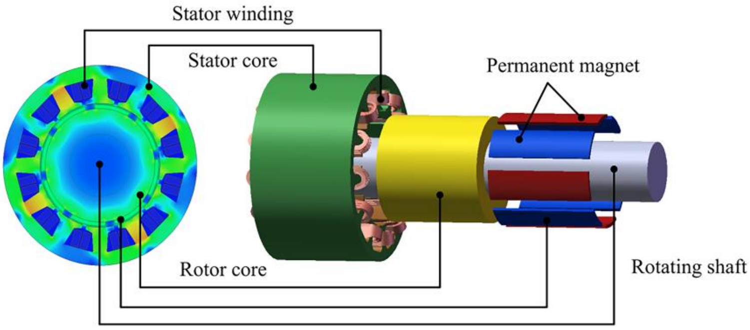

Fig. 1. Representation of wound sample for experimental analysis

As is well known, stray losses are caused by time harmonic currents, magnetic field asymmetry, mechanical motion imbalance, and defects in motor design and manufacturing processes. Mechanical losses are caused by wind resistance losses and bearing friction losses, making it difficult for electromagnetic calculation software and analysis models to calculate accurately. Based on design experience and considering the power level, voltage level, speed, and manufacturing process of the concept verification PMSM motor, stray losses are selected at 0.7% of the rated output power, and mechanical losses are selected at 0.5% of the rated output power.

Table 1. Design structure of the concept verification PMSM motor

Parameters	**Values**
Rated power P_N (kW)	40
Rated speed n_N (r/min)	600
Rated voltage U_N (V)	380
Rated frequency f (Hz)	50
Outer diameter of stator D_{so} (mm)	360
Length of iron core L_a (mm)	215
Inner diameter of stator D_{si} (mm)	223
Number of stator slots Z	12
Number of pole pairs P	4
Rated power factor $\cos\varphi$	0.93
Maximum operating temperature under insulation level T (°C)	130
Rated efficiency η (%)	96.2
Maximum torque $T_{\max}$ (N·m)	1019

Based on the prototype design of the PMSM motor, this paper presents a direct cooling thermal management approach utilizing a wrap-around configuration to enhance torque output capacity while accounting for thermal constraints. The stator slot adopts a hybrid winding setup, where two hollow cooling tubes are positioned diagonally alongside two copper windings. Additionally, four hybrid windings are placed in parallel around the stator teeth. A diagram of this cooling technique is shown in Fig. 2.

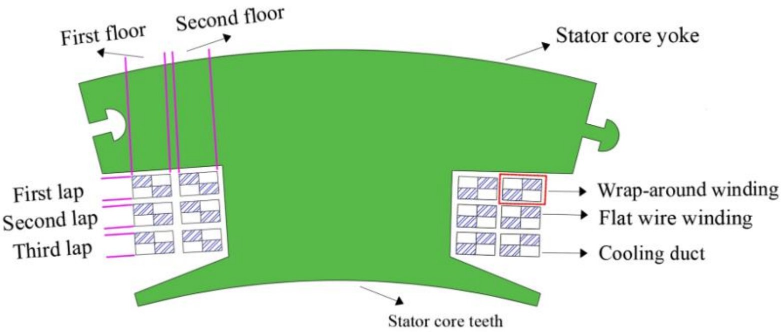

Fig. 2. Illustration of the direct cooling scheme for wrap-around systems

The companion windings are configured using a parallel winding method, as illustrated in Fig. 3. The process starts with the simultaneous winding of the cooling tube and copper winding from the bottom slot of the stator, ascending along the right side of the stator teeth and reaching the slot on the opposite left side. After completing a full circuit, the companion windings are shifted to a specific height at the stator's end before descending to begin the next round. Upon finishing the first layer of windings, the second layer is initiated by winding the first circuit parallel to the inclined shoulder of the stator slot. Once the first circuit of the second layer is done, the winding process continues upward, maintaining a consistent height at the stator's end, until all four companion windings of the second layer are wound [1].

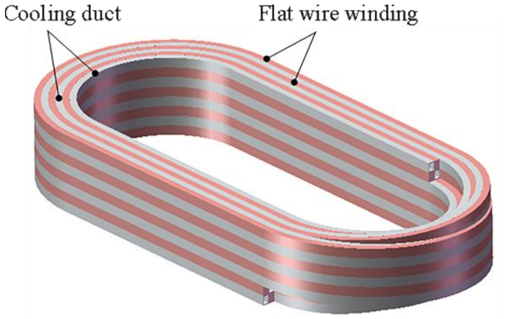

Fig. 3. Schematic diagram of parallel winding of wrap-around windings

As shown in Fig. 3, the tubes between the layers and laps are in contact both within the stator slot and at the stator end. Additionally, several surfaces of the copper winding are in direct contact with the cooling tubes, making the winding appear as though it is immersed in coolant.

According to the operational performance of the concept verification PMSM motor and the proposed thermal management strategy, an epoxy resin encapsulation is chosen as the insulating material between the copper winding and the cooling medium, with thermal conductivity parameters of 1.2 W/m·K. For the stator slots, a polyester film composite insulation paper, rated at insulation grade E, is utilized, offering thermal conductivity parameters of 0.138 W/m·K.

Due to the mutual suppression and cancellation of the induced potential formed on the surface of the copper conductor around the cooling pipe, the eddy current loss on the surface of the cooling pipe only accounts for 0.1% of the output power of the concept verification PMSM motor. The eddy current loss generated has a relatively small impact on the normal operation of the motor. In order to reduce the complexity of the analysis model proposed in this article, the eddy current loss of the cooling pipe will be ignored in subsequent research.

3. Establishment of three-dimensional thermal network model

To quickly and accurately demonstrate the feasibility and efficiency of the proposed thermal management approach, this section introduces a three-dimensional thermal network analysis model. Specifically focusing on the wrap-around liquid-cooled scheme, the paper presents a discrete axial-radial LPTN model, illustrated in Fig. 4. The LPTN depicted in Fig. 4 solely accounts for heat transfer in the radial-axial plane, while the wrap-around liquid-cooled scheme proposed in this study significantly impacts heat transfer of the circumferential plane in both the copper windings and the stator core. Additionally, the heat transfer anisotropy of different motor components further affects circumferential heat flow. Consequently, to more accurately estimate the temperature increment in each component for the wrap-around liquid-cooled motor, a LPTN model that incorporates circumferential heat dissipation is developed, as shown in Fig. 5. For simplicity, only the radial-circumferential LPTN model for the stator slots and hybrid winding is displayed.

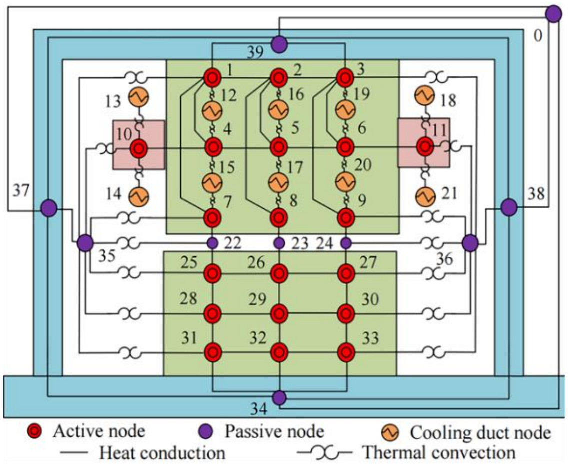

Fig. 4. Axial-radial LPTN model diagram for wrap-around liquid-cooled scheme

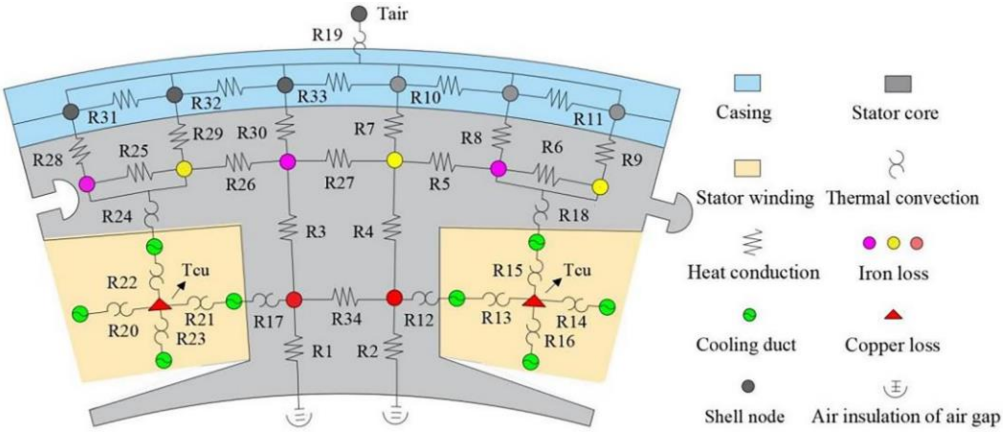

Fig. 5. Radial-circumferential LPTN model diagram of wrap-around liquid-cooled motor

To balance computational accuracy with minimizing computational costs, a sensitivity analysis of the 3D LPTN model was conducted. The analysis followed the steps outlined below:

1. The isothermal nodes, defined as those with temperatures within ±1°C, are consolidated.
2. Only nodes representing the hot-spot temperatures are retained for each machine's segment.
3. The calculation of equivalent resistances is accomplished through the application of series and parallel circuit formulas.

The axial-radial and radial-circumferential LPTN models for the wrap-around liquid-cooled motor, obtained through sensitivity analysis, contain a larger number of nodes. To present a clearer and more straightforward depiction of the heat source distribution and the thermal resistance configuration in this cooling system, Figs. 4 and 5 display only the three-dimensional thermal network of the wrap-around liquid-cooled motor, without showing all the nodes.

For the sub model of the heating network, this paper adopts a higher grid density for areas with dense heat sources, such as windings, iron cores, and permanent magnets, in order to more accurately capture heat transfer and temperature distribution. However, for areas with small thermal gradients (such as the casing and shaft), this article uses a lower grid density to balance computational accuracy and efficiency. At the same time, due to the use of different materials for different components of the motor, the thermal conductivity, specific heat capacity, and density parameters of each material are different. Therefore, this article calculates and analyzes different grid densities for different materials.

For the magnetic mesh sub model, due to the drastic changes in the magnetic field in the air gap, this paper finely processes the grid density in the air gap region to better capture the distribution and conduction characteristics of the magnetic field. However, in the stator or rotor core region, due to the relatively gentle changes in the magnetic field, this article selects a coarser grid for this area. Based on the stator or rotor core region, this article also uses finer grids to improve the accuracy of magnetic field calculations for areas prone to magnetic saturation, transition regions between magnetic poles and rotor cores, and transition regions between stator windings and stator cores.

By conducting independent analysis on the thermal network sub model and the magnetic network sub model, the final grid size and density of the two sub models are determined for the establishment and analysis of the electromagnetic loss-node temperature-thermal parameter coupling model in the future.

4. Establishment of electromagnetic loss-node temperature-thermal parameter coupling model

Given the intricate coupling of multiple physical fields within a motor, an accurate prediction of the temperature distribution across each component in the wrap-around liquid-cooled system requires a more comprehensive approach. To achieve this, a thermal evaluation model that integrates electromagnetic loss, node temperature, and thermal parameters is developed based on a three-dimensional thermal network framework.

4.1. Coupling relationship between electromagnetic loss and temperature rise

This section examines the relationship between electromagnetic losses and motor temperature rise, providing a theoretical basis for developing a coupling model that links electromagnetic loss, nodal temperature, and thermal parameters.

4.1.1. Copper loss of windings at different temperatures

The stator winding's resistivity varies with temperature. The temperature-resistance relationship for each phase of the stator winding is determined using (1) [23].

$$R = \rho_{20}[1 + \alpha_{\text{cu}}(t - 20)]\frac{2N_w L_{\text{av}}}{aA_s}, \tag{1}$$

where ρ_{20} is the resistivity of copper at 20° and α_{cu} is the temperature coefficient, A_s is the cross-sectional area of the winding, L_{av} is the average half-turn length of the coil, a is the number of parallel branches, and N_w is the number of turns in series per phase.

Therefore, the variation of copper loss of stator windings with temperature can be calculated according to (2) [23].

$$P_{\text{cu}} = 3I^2 K_r R, \tag{2}$$

where K_r is the resistance increase coefficient introduced by the skin effect of the stator winding.

4.1.2. Core loss at different temperatures

At present, NdFeB magnet is widely used in PMSMs, but its thermal stability is poor, and the change rate of magnetic performance with temperature is relatively large. The residual magnetic induction B_t of the permanent magnet at different temperatures can be calculated by (3) [24].

$$B_t = \left[1 - \frac{(t - 20)\,\alpha_{Br}}{100}\right]\left(1 - \frac{IL}{100}\right)B_{20}. \tag{3}$$

Therefore, the variation of flux density amplitude B_m with temperature can be solved according to (4) [24].

$$B_m = \frac{b_{mo}(t)B_t A_m \times 10^4}{\sigma_0 \alpha_i \tau_i L_{ef}}, \tag{4}$$

where $b_{mo}(t\ )$ is the no-load working point of the permanent magnet varying with temperature, A_m is the flux area per pole, σ_0 is the no-load magnetic flux leakage coefficient, α_i is the calculated polar arc coefficient, τ_i is the polar distance, and L_{ef} is the calculated length of the armature.

$$P_{\text{Fe}} = k_h f B_m^a + k_e f^2 B_m^2 + k_{\text{exc}} f^{1.5} B_m^{1.5}, \tag{5}$$

where the coefficients k_h, k_e and k_{exc} are derived from the loss curve fitted as indicated by the manufacturer.

4.1.3. Eddy current loss of permanent magnet at different temperatures

The eddy current losses in a loaded PM can be determined using the conventional formula for eddy current loss, as presented in (6) [25].

$$P_w = \frac{1}{24}\sigma\omega^2 d^2 B_{\text{av}}^2 F\left(\frac{d}{\Delta}\right), \tag{6}$$

where σ is the conduction parameter of PM, ω is the frequency of rotating magnetic field, d is the magnetic field direction length of the PM, B_{av} is the average magnetic flux density, and Δ is the skin depth, $\Delta = \sqrt{\frac{2}{(\omega\mu\sigma)}}$.

Because the conductivity of the permanent magnet varies with temperature, the eddy current loss of the PM at different working temperatures can be calculated by calling the conductivity at different temperatures in the model program.

4.2. Coupling relationship between node temperature and thermal parameters

The conduction parameter of copper and insulating materials varies with temperature as shown in (7) and (8) [26], respectively. It can be seen that the conduction parameter of copper and insulating materials decreases with the temperature increment.

$$\lambda_{\mathrm{cu}} = 345.125 - 0.125t, \tag{7}$$

$$\lambda_{ins} = 0.36946 - 0.000362t. \tag{8}$$

The cooling tube material selected in this paper is 304 stainless steel, and the relationship between conduction parameter and temperature is shown in (9) [27]. The conduction parameter of the cooling tube material rises as the temperature increases.

$$\lambda_{304} = 16.2 + 0.037t. \tag{9}$$

The equivalent thermal conductivity of silicon steel laminates varies proportionally at different interface temperatures, and the relationship is shown in (10) [28]. The equivalent thermal conductivity of silicon steel sheets is observed to decline as the average interface temperature rises.

$$\lambda_d = 1.4(t)^{-0.222} + 2.971. \tag{10}$$

At present, the rotating shaft is mostly made of No. 45 round steel, and its thermal conductivity varies with temperature as shown in (11) [29]. It can be seen that the thermal conductivity of the rotating shaft material decreases with the increase in temperature.

$$\lambda_{45} = 50.215 - 0.046t. \tag{11}$$

When the water medium flows in the cooling tube, due to the change of water temperature, its kinematic viscosity, thermal conductivity, density, specific heat capacity and other parameters change dynamically, thus affecting the convective heat dissipation coefficient of the inner wall surface of the cooling tube.

4.3. Electromagnetic loss-node temperature-thermal parameter coupling model

In this paper, a coupling scheme between electromagnetic loss, node temperature, and thermal parameters is developed based on the analysis of their interrelations. As shown in Fig. 6, the electromagnetic loss of the PMSM is utilized as a heat source for the three-dimensional thermal network model. The temperature rise data from the thermal field is fed back to update the loss data. Simultaneously, the average node temperature of each component in the network is linked with the thermal parameter library, updating the thermal parameters. This approach makes the coupling calculation more accurately reflect the motor's actual temperature rise process.

MATLAB software was utilized to develop an electromagnetic calculation program for the PMSM, and a 3D thermal network model was constructed. Two separate databases were created for

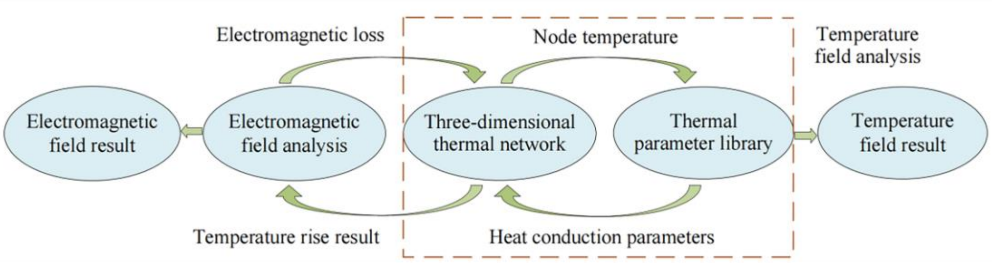

Fig. 6. Coupling scheme of electromagnetic loss-node temperature-thermal parameter

the coupling calculations. One database specifically stores thermal parameters at various temperatures, as provided by the manufacturer, while the least squares method was employed to model the relationship between thermal parameters and temperature. Figure 7 illustrates the process flow of the coupling calculations between electromagnetic losses, node temperature, and thermal parameters.

At the beginning of the coupling calculation, the electromagnetic program is called to calculate the electromagnetic loss value P_n at the ambient temperature. Then the 3D thermal network model is called, and the loss value at the ambient temperature is used as the heat source to calculate the node temperature value T_n of different components. Then the thermal parameter λ_n under the node temperature value T_n is called for use in the next iteration. At this time, the electromagnetic program is called again to calculate the electromagnetic loss value P_{n+1} under the average node temperature T'_n. The heat transfer parameter λ_n is used to update the thermal resistance and calculate the node temperature value T_{n+1} of the motor component under the loss value P_{n+1}. The highest node temperature T''_n and T''_{n+1} values in the same component are compared, and the feedback module is added and the corresponding convergence conditions are set. In order to evaluate the accurate steady-state temperature values of different components, the convergence condition of coupling calculation is $T''_{n+1} - T''_n \leq b0.3 \cdot bK$ in each component. If the error of the two adjacent temperature rise simulation results of the electromagnetic loss-node temperature-thermal parameter coupling model satisfies the preset convergence condition, the coupling calculation ends and the steady-state temperature value of each component is output. If it is not satisfied, the calculation is continued, that is, the final temperature rise result satisfying the convergence condition is obtained by iterative calculation.

It is well known that the entire motor consists of several different components, whereas in a three-dimensional thermal network model, the same component consists of multiple nodes.

It should be noted that the coupling calculation process described above is described for one of the components. T_n and T'_n are the temperature of one node and the average temperature of multiple nodes respectively. When the thermal parameter is called, the thermal parameter λ_n under a node temperature T_n is called. However, when the electromagnetic loss is iteratively calculated, the loss value P_{n+1} under the average temperature T'_n of different nodes in the same component is calculated. In the thermal evalution of the motor, we are concerned about the highest temperature of each component of the motor, rather than the average temperature. Therefore, after the iteration of the coupling calculation, the coupling model established in this paper outputs the highest node temperature T''_{n+1} in the component.

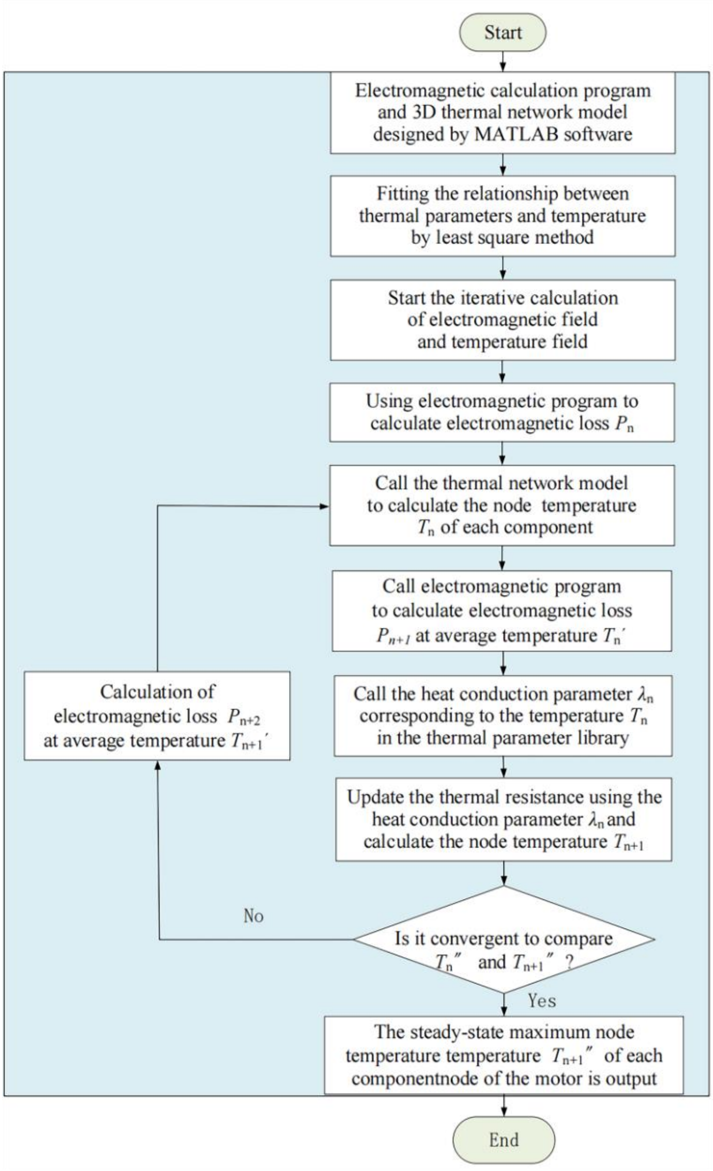

Fig. 7. Flow chart of calculation of electromagnetic loss-node temperature-thermal parameters

In order to use the least square method to fit the optimal polynomial function between thermal parameters and temperature, polynomial function fitting of different orders is performed according to multiple data points provided by the manufacturer, and the residual sum of squares and the R sum of squares of polynomial functions of different orders are calculated. If the residual sum of squares is the smallest and the R sum of squares is the largest, the fitting degree of polynomial function under the corresponding order is higher, which can be used as the thermal parameter library in the coupling model established in this paper to call the thermal parameter values at different temperatures during heating evaluation.

To efficiently and accurately determine whether the temperature rise of each motor component exceeds the permissible limit during continuous operation, the coupling model used in this study omits the specific heat capacities of the materials and disregards the variation in temperature rise over time. Instead, it focuses solely on calculating the temperature values of each motor component once thermal equilibrium is achieved.

5. Verification of coupling model and thermal management scheme

5.1. Verification of coupling model

Since the FEA-CFD bidirectional coupling model can accurately simulate the temperature distribution of each motor component during actual operation, it is considered the benchmark model. To evaluate the advantages of the coupling model proposed in this paper, in terms of prediction accuracy and computational cost, comparisons are made between the FEA-LPTN, FEA-FEA models, and the proposed coupling model with the FEA-CFD bidirectional model. Additionally, the energy consumption of the cooling system at various cooling water temperatures is roughly estimated. During the thermal evaluation of the concept verification PMSM motor, the optimal cooling water temperature at a given ambient temperature is determined by minimizing the total power consumption, which includes the motor's power use, the cooling system's energy consumption, and the cooling efficiency.

Given that the FEA-CFD coupling model can effectively replicate the temperature distribution across various motor components during actual operation, this paper aims to validate the accuracy of the proposed coupling model. To do so, a 40 kW PMSM motor is selected as the physical model, and the resulting temperature distribution of each motor component is illustrated in Fig. 8. In addition, references [12, 16] also established the FEA-LPTN coupling model and the FEA-FEA coupling model respectively. To determine the maximum temperature of each motor component during finite element analysis, a tetrahedral mesh element was applied in the model. During the structural mesh refinement process, the size and number of mesh elements were manually adjusted both locally and globally, based on the temperature distribution results obtained from the finite element analysis. This adjustment aimed to enhance calculation precision. The final optimized mesh quality parameters were as follows: a skewness of 0.6, a cell size variation of 1, an aspect ratio of 4:1, and a total of 2 085 286 mesh elements.

Under identical ambient temperature and cooling medium conditions, a comparison was conducted between the analysis results of the electromagnetic loss-node temperature-thermal parameter coupling model and the FEA-LPTN, FEA-FEA, and FEA-CFD coupling models. The motor loss calculation results are provided in Table 2.

As shown in Table 2, the coupling model for electromagnetic loss, node temperature, and thermal parameters presented in this paper indicates higher copper loss in the windings compared to the FEA-LTPA and FEA-FEA models. This is because the proposed model accounts for the temperature-dependent changes in thermal parameters, leading to a decrease in the thermal conductivity of copper, insulating paper, and silicon steel as temperature rises. While the cooling

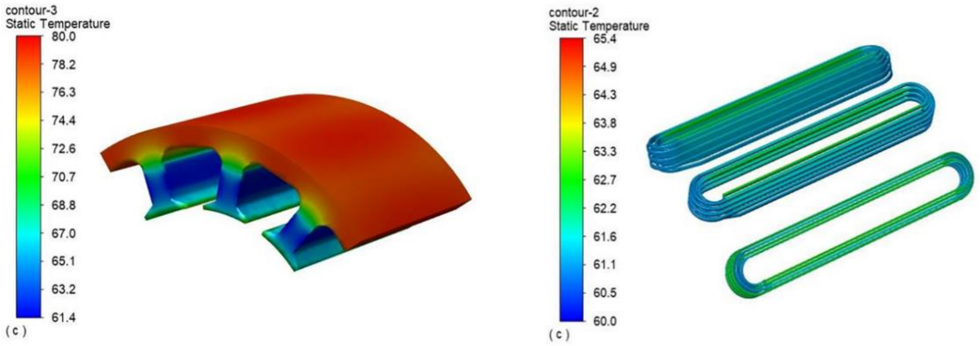

(a) Stator core (b) Wrap-around winding

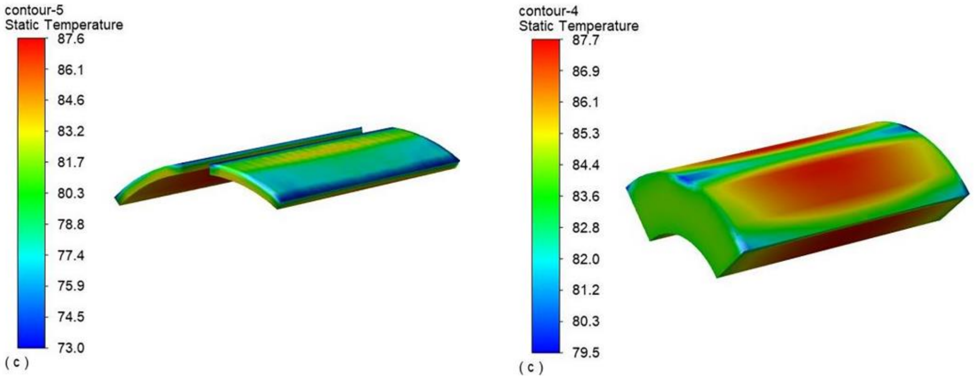

(c) Permanent magnet (d) Rotor core

Fig. 8. (Temperature distribution diagram of various components of wrap-around liquid-cooled motor based on the FEA-CFD coupling model

Table 2. Calculation results of motor loss with different coupling models

Coupling model	**FEA-LPTN**	**FEA-FEA**	**The model proposed in this article**	**FEA-CFD**
Copper loss (W)	617.8	631.7	674.4	665.2
Stator iron loss (W)	491.3	481.7	466.3	469.8
Eddy current loss (W)	174.6	167.5	155.1	158.9
Rotor iron loss(W)	27.8	25.7	22.6	23.9

duct's thermal conductivity rises with temperature, the rate of change is minimal, preventing efficient heat transfer from the stator winding. Additionally, the resistivity of the winding increases, leading to higher copper losses. The rotating shaft's thermal conductivity decreases with temperature, slowing the dissipation of heat generated by rotor iron and eddy current losses in the permanent magnet, further weakening its magnetic properties. As the temperature increases, the magnetization of the silicon steel sheet decreases slightly due to its effect on the permanent magnet flux and the overall electromagnetic field. Consequently, the flux density of the stator and rotor cores diminishes, leading to a reduction in both rotor core loss and permanent magnet eddy current loss.

The temperatures of various motor components calculated using different coupling models are displayed in Fig. 9.

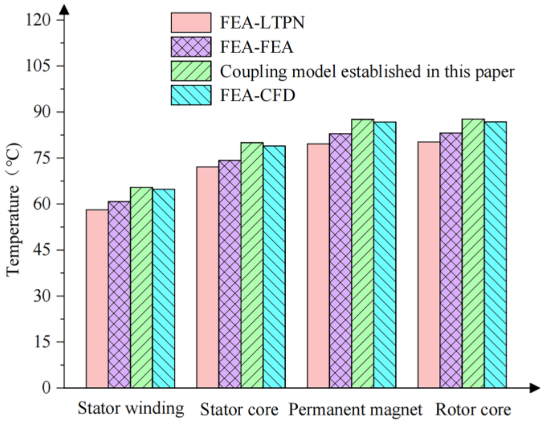

Fig. 9. Temperature of motor components calculated by different coupling models

It is evident that the winding temperature experiences a significant rise, primarily due to the sharp increase in copper losses. Since copper loss serves as the primary heat source, the electromagnetic loss-node temperature-thermal parameter coupling model results in a higher overall motor temperature compared to the FEA-LTPA and FEA-FEA coupling models. Since the coupling model in this paper doesn't account for the dynamic changes in the convection coefficient on the cooling tube wall surface or the air convection in the motor's air cavity, there is a prediction error in the motor's component temperatures when compared to the FEA-CFD model. Table 3 presents a comparison of the relative error, computation time, and resource usage of the FEA-LPTN model.

Table 3. Comparison of calculation time, physical memory and relative error

Method	**Relative error**	**Calculation time**	**Physical memory**
The model established in this paper	1.1	0.16	0.35
FEA-LPTN	8.5	0.28	0.59
FEA-FEA	5.3	1.33	1.48
FEA-CFD	/	4.2	4.8

As shown in Table 3, the coupling model proposed in this paper demonstrates the lowest relative error and superior calculation accuracy compared to the FEA-LPTN and FEA-CFD models. While the FEA-CFD model effectively predicts the motor's temperature rise distribution, both FEA and CFD rely on finite element and finite volume methods to partition the computational domain into distinct units or volumes. These methods convert a continuous problem with infinite degrees of freedom into a discrete one with finite degrees of freedom by integrating each control unit or volume through the differential equation. Given the specific solution method and mesh convergence technology of the FEA-CFD coupling model, enhancing the model's calculation accuracy requires dividing the complex physical model into numerous meshes. This, however, demands significant physical memory and prolongs computation time, hindering the rapid development of new motor products in practical engineering projects. In this paper, the coupling model or LPTN breaks down the research object's physical model into unit nodes. Energy transfer occurs between nodes, where magneto or thermal resistance replaces the nodes. By applying KCL and KVL laws from electrical theory, equilibrium equations for electromagnetic and heat transfer problems are derived. The coupling model proposed in this paper simplifies both the physical model and algorithm of the motor, resulting in reduced computation time and cost, with the simulation time being just 3.8% of that required by the FEA-CFD coupling model. Furthermore, the relative error is only 1.1%, ensuring high accuracy. This approach allows for rapid and precise identification of the motor's hottest spot during operation, facilitating motor design and optimization in real-world engineering applications.

The stator winding temperature with cooling water ranging from 25°C to 35°C is calculated using both the coupling model presented in this paper and the FEA-CFD coupling model. The error between the two models remains around 1.1%. This shows that the accuracy of the coupling model proposed in this paper is unaffected by changes in cooling water temperature.

In order to verify the influence of temperature on the characteristics and thermal parameters of electromagnetic materials, this paper also established a coupling model (defined as coupling model 1) that did not consider the influence of temperature on the characteristics and thermal parameters of electromagnetic materials. At the same time, it was compared with the coupling model considering the influence of temperature on the characteristics and thermal parameters established in Section 4 of this paper (defined as coupling model 2) and the FEA-CFD coupling model. The temperature of different motor components in the wrap-around liquid-cooled scheme based on three coupling models was compared, as shown in Fig. 10.

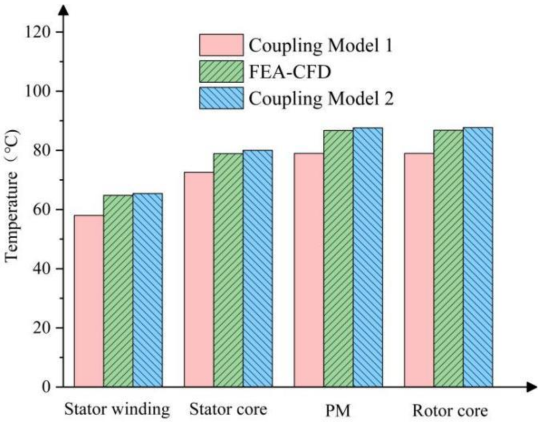

Fig. 10. Temperature of different motor components in wrap-around liquid-cooled scheme based on three coupling models

According to Fig. 10, the relative error between coupling model 1 and FEA-CFD coupling model is 8.1%, which is relatively large. The relative error between coupling model 2 and FEA-CFD coupling model is 1.1%, which is relatively small. The reason for this is that compared to coupling model 2, the electromagnetic material properties and thermal parameters in coupling model 1 are fixed and unchanged at different temperatures. However, actual temperature changes can significantly affect the electromagnetic properties and thermal behavior of materials, thereby affecting the overall system's thermal distribution and response. Therefore, the calculation results of coupling model 2 and FEA-CFD coupling model are consistent, further verifying the feasibility and accuracy of the electromagnetic loss-node temperature-thermal parameter coupling model proposed in this paper.

5.2. Verification of thermal management scheme

Using a 40 kW PMSM motor as a case study, this paper employs the proposed coupling model along with the FEA-CFD coupling model to assess the indirect casing cooling approach. The temperatures of various motor components, as calculated by both models, are presented in Fig. 11. Additionally, the relative error, computation time, and resource consumption for both coupling models are analyzed and compared.

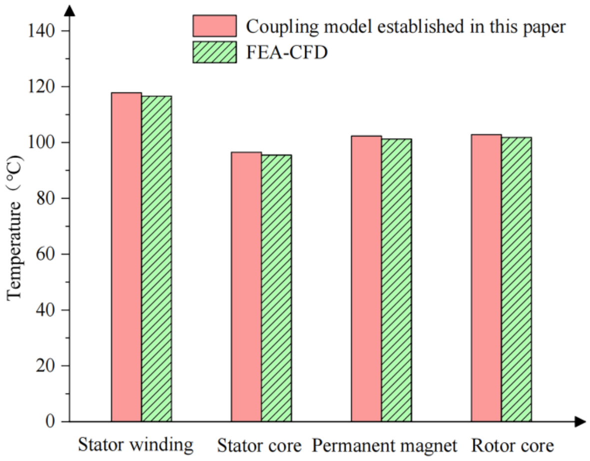

Fig. 11. Component temperature of indirect casing cooling motor calculated by two coupling models

Based on the analysis and statistics of Fig. 11 and related parameters, the coupling model proposed in this study demonstrates high accuracy in predicting the thermal performance of indirect casing cooling schemes. The relative error compared to the FEA-CFD coupling model is merely 1%. Moreover, the simulation time is significantly shorter, accounting for just 3.6% of the FEA-CFD model's runtime. This reduction in both computational time and cost underscores the model's effectiveness and precision in evaluating indirect casing cooling schemes.

At the same slot filling rate and number of conductors per slot, the cross-sectional area of each turn of stator winding based on the wrap-around liquid-cooled scheme is half that of the indirect casing cooling scheme. In order to compare the heat dissipation capabilities of two thermal management schemes under the same stator winding cross-sectional area (copper share), the concept verification of PMSM motor based on the original cooling scheme (the indirect casing cooling scheme) is defined. The cross-sectional area of the stator winding in PMSM motor is S, and the cross-sectional area of the stator winding of the motor based on the proposed wrap-around liquid-cooled is 1/2S. Under the same load and cooling medium parameters, the temperature of each component of the motor was calculated and compared between the wrap-around liquid-cooled (stator winding cross-sectional areas S and S/2) and indirect casing cooling (stator winding cross-sectional areas S and S/2) thermal management schemes. The results are shown in Fig. 12.

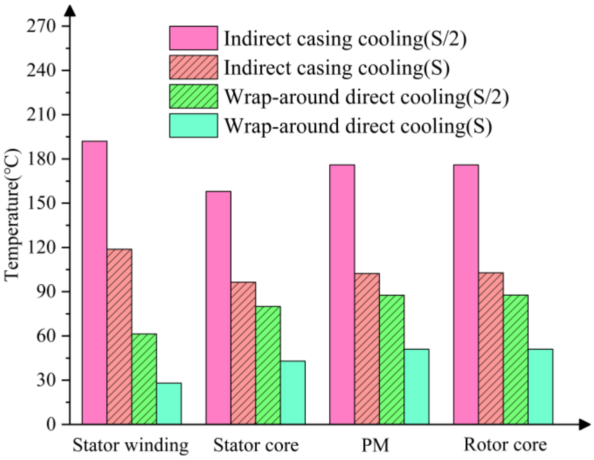

Fig. 12. Temperature comparison of various components of motor with wrap-around liquid-cooled and indirect casing cooling

From Fig. 12, it can be seen that the temperature of the stator winding based on the wrap-around liquid-cooled motor (stator winding cross-sectional area S/2) is 34.1% of that based on the indirect casing cooling motor (stator winding cross-sectional area S/2), and 55.5% of that based on the indirect casing cooling motor (stator winding cross-sectional area S). Meanwhile, the temperature of the stator winding based on the wrap-around liquid-cooled motor (stator winding cross-sectional area S) is 23.8% of that based on the indirect casing cooling motor (stator winding cross-sectional area S). The main reason for this is that the cooling pipes in the wrap-around liquid-cooled scheme are in direct contact with multiple surfaces of the winding, minimizing the thermal resistance between the winding hotspots and the cooling medium. This can quickly extract the heat generated by the entire winding, thereby improving the heat dissipation capacity of the motor and ultimately reducing the overall temperature rise level of the motor.

Although the cooling channels in the wrap-around liquid-cooled scheme reduce the copper cross-section in the slot, thereby increasing the winding resistance. However, as shown in Fig. 12, the temperature of different components based on the wrap-around liquid-cooled scheme is much lower than that based on the indirect casing cooling scheme. Moreover, the copper conductivity of the stator winding, the magnetic permeability of the stator or rotor core, and the remanence and coercivity of the permanent magnet exhibit nonlinear laws with temperature changes, which affect the losses of different components of the motor. Therefore, by using the electromagnetic loss-node temperature-thermal parameter coupling model established in this paper, the efficiency value based on the wrap-around liquid-cooled scheme is reduced by 0.6% compared to the indirect casing cooling scheme. It can be seen that the wrap-around liquid-cooled scheme has a relatively small impact on the operating efficiency of the motor while efficiently reducing the temperature rise of different parts of the motor.

6. Test verification of mock-up model

To enable the testing and verification of the cooling performance in the companion direct cooling scheme, a mock-up model structure was created. This model incorporates the stator core design, wrap-around winding, and casing, as illustrated in Fig. 13. Additionally, for comparative verification against the wrap-around liquid-cooled system, another mock-up model was devised for the indirect casing cooling method. In this design, a cooling tube is coiled around the axis of the casing, following the circular groove, as depicted in Fig. 14.

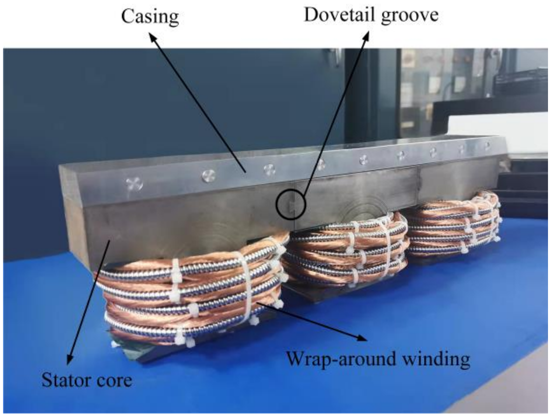

Fig. 13. Mock-up model of the wrap-around liquid-cooled scheme

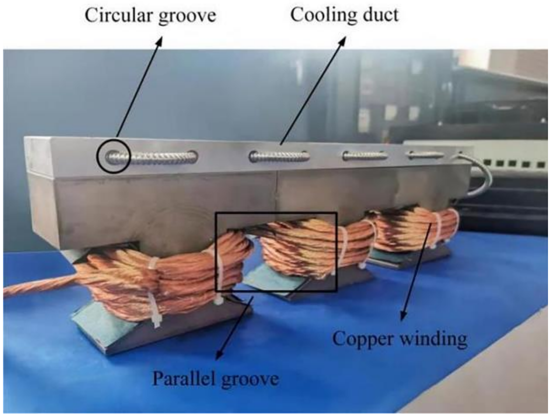

Fig. 14. Mock-up model of indirect casing cooling scheme

The experimental setup for testing both the wrap-around liquid-cooled and indirect casing cooling schemes is illustrated in Fig. 15. To achieve precise temperature measurements of various components within the mock-up model, nine PT100 sensors were strategically placed along the circumferential direction on both the front and back outer surfaces of the casing, which interact with the external environment. Additionally, two PT100 sensors were mounted along the axial direction on both the left and right sides of the casing. Nine PT100 sensors were mounted circumferentially, and two were mounted axially on the upper surface of the casing. On the stator yoke's front and back surfaces, in contact with the external environment, nine PT100 sensors were placed circumferentially, and two were positioned radially.

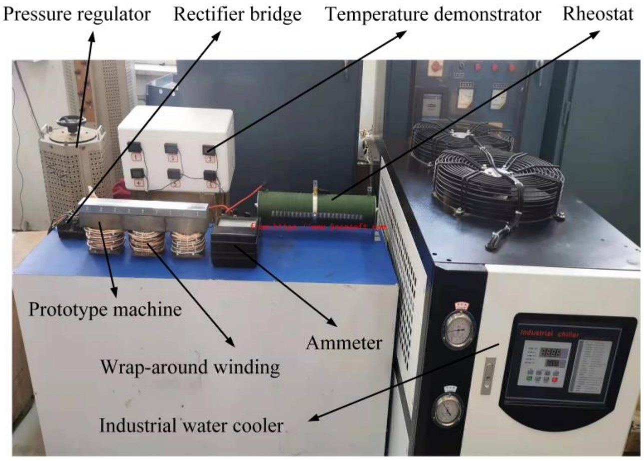

Fig. 15. Testing equipment for two cooling schemes

Two PT100 sensors are positioned axially on both the left and right sides of the stator yoke, with an additional two sensors placed radially. On the two outer surfaces of the stator core teeth, which are exposed to the external environment, PT100 sensors are mounted on the front and back surfaces along the circumferential direction, and three more are placed radially. Within each stator slot winding, two PT100 sensors are embedded circumferentially, and three sensors are installed radially on both sides of the winding end. Additionally, three PT100 sensors are embedded radially in the two layers of the winding inside the slot, along with two sensors axially and two circumferentially. Some of the PT100 sensors in the stator winding are embedded on the surface where the winding contacts the stator core. Simultaneously, the highest temperature areas of various components in the mock-up model are visually identified using a temperature display. During subsequent measurements, focus is placed on the display value at the hottest point for each component, with the recorded value taken as the steady-state temperature. In the experiment, an industrial water cooler is employed to lower the temperature of the water medium, while the copper winding within the hybrid winding is powered by a three-phase auto-voltage regulator and rectifier bridge to supply the test current.

To verify the prediction accuracy of the coupling model developed in this paper and assess the cooling efficiency of the wrap-around liquid-cooled scheme, the model is applied to simulate mock-up models under two thermal management approaches. A comparative coupling analysis is conducted, and the simulation results from both schemes are compared against experimental data. At an ambient temperature of 15°C, the same cooling medium inlet temperature and flow rate are set for testing and simulation under the two thermal management scenarios. Figure 16 shows the emulation analysis and experimentation results of the mock-up model based on the two thermal management schemes. In order to prevent the cooling water temperature difference between the inlet and outlet of the cooling tube from being too large and causing temperature gradients in different directions of the motor, the temperature difference between the inlet and outlet cooling water is 3 ° by controlling the flow rate of the cooling water in the mock-up experiment.

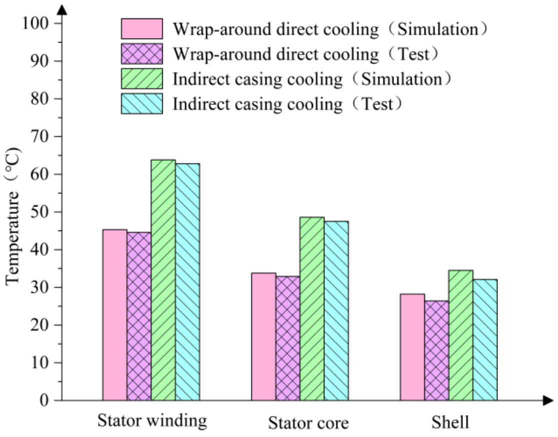

Fig. 16. Comparison of simulation and experimental values based on two heat management schemes

As shown in Fig. 16, the simulation results of the mock-up model for both thermal management schemes closely match the test data. This confirms the accuracy of the proposed electromagnetic loss-node temperature-thermal parameter coupling model for motor thermal analysis. Additionally, Fig. 16 demonstrates that the winding temperature rise in the wrap-around liquid-cooled scheme is 18.5 K lower than in the indirect casing cooling scheme, further proving the superior heat dissipation capability of the direct cooling approach for the winding.

The critical factor in motor operation is the highest temperature point. Therefore, the peak temperature in FEA, CFD, and mock-up models is compared with the highest node temperature in the LPTN or the coupling model developed in this study.

7. Conclusion

Based on the restrictions imposed by the thermal limits on the torque output capacity of motors, a cooling scheme of wrap-around liquid-cooled is proposed in this paper. According to the 3D thermal network model, a magneto-thermal coupling model of electromagnetic loss-node temperature-thermal parameters is established to evaluate the thermal performance of an example motor, and compared to the thermal management scheme using indirect casing cooling. The conclusions are as follows:

1. Through the simulation comparison between different coupling models and FEA-CFD coupling model, the relative error of the coupling analysis system established in this paper is only about 1.1%. Simultaneously, the simulation calculation time of the coupling model established in this paper is only 3.8% of that of the FEA-CFD coupling model, which greatly reduces the calculation time cost and computing resources on the premise of improving the accuracy of motor thermal evaluation, which is beneficial to reduce the design and optimization cycle of the motor in engineering practice.
2. By simulating and comparing the wrap-around liquid-cooled and indirect casing cooling schemes using the coupling model developed in this study, it is found that the peak winding temperature in the wrap-around liquid-cooled motor is 72% of that in the indirect casing cooling motor. This indicates a more effective thermal management solution, enhancing the motor's torque output capacity.
3. This study not only shortens the thermal evaluation cycle for the design and optimization of new motor products, but also improves the thermal safety factor of the motor in actual operation.

Acknowledgements

This work was supported by the Science and Technology Major Projects of Liaoning Province, China (Grant No. 2023JH1/11100010).

References

[1] Hou Q. *et al.*, *Evaluation and test of impact-resistant overload capability of companion-type direct cooling motor*, IEEE Access, vol. 11, pp. 126295–126311 (2023), DOI: 10.1109/ACCESS.2023.3257996.

[2] Krok R., *Influence of work environment on thermal state of electric mine motors*, Archives of Electrical Engineering, vol. 60, no. 3, pp. 357–370 (2011), DOI: 10.2478/v10171-011-0031-6.

[3] Feng J., Tan D., Yuan M., *Influence of road excitation on thermal field characteristics of the water-cooled IWM*, Archives of Electrical Engineering, vol. 70, no. 3, pp. 689–704 (2021), DOI: 10.24425/aee.2021.137582.

[4] Yin Y., Li H., Xiang X., *Oil Friction Loss Evaluation of Oil-Immersed Cooling In-Wheel Motor Based on Improved Analytical Method and VOF Mode*, World Electric Vehicle Journal, vol. 12, no. 4 (2021), DOI: 10.3390/wevj12040164.

[5] Liu C., Zou J., Xu Y., Yu G., *An Efficient Thermal Computation Model of PMSM Based on FEA Results and Interpolation*, IEEE Trans. Appl. Supercond., vol. 31, no. 8, pp. 1–4 (2021), DOI: 10.1109/TASC.2021.3096512.

[6] Acquaviva A., Wallmark O., Grunditz E.A., Lundmark S.T., Thiringer T., *Computationally Efficient Modeling of Electrical Machines with Cooling Jacket*, IEEE Trans. Transport. Electrific., vol. 5, no. 3, pp. 618–629 (2019), https://ieeexplore.ieee.org/abstract/document/8805130.

[7] Jin L., Mao Y., Wang X., Lu L., Wang Z., *A Model-Based and Data-Driven Integrated Temperature Estimation Method for PMSM*, IEEE Trans. Power Electron., vol. 39, no. 7, pp. 8553–8561 (2024), DOI: 10.1109/TPEL.2024.3382300.

[8] Wang Xiaoyuan, Li Na, Li Tianyuan, Xu Yuhao, *Electromagnetic design of an ultra-high-speed bearingless permanent magnet synchronous motor*, IET Electr. Power Appl., vol. 18, no. 3, pp. 287–296 (2023), DOI: 10.1049/elp2.12388.

[9] Min S.G., Sarlioglu B., *3-D Performance Analysis and Multiobjective Optimization of Coreless-Type PM Linear Synchronous Motors*, IEEE Trans. Ind. Electron., vol. 65, no. 2, pp. 1855–1864 (2018), DOI: 10.1109/TIE.2017.2745475.

[10] Attila Nyitrai, Miklós Kuczmann, *Magnetic equivalent circuit and finite element modelling of anisotropic rotor axial flux permanent magnet synchronous motors with fractional slot distributed winding*, IET Electr. Power Appl., vol. 17, no. 5, pp. 709–720 (2023), DOI: 10.1049/elp2.12298.

[11] Zhao W., Cao D., Ji J., Huang L., Liu T., *A Generalized Mesh-Based Thermal Network Model for SPM Machines Combining Coupled Winding Solution*, IEEE Trans. Ind. Electron., vol. 68, no. 1, pp. 116–127 (2021), DOI: 10.1109/TIE.2020.2965484.

[12] Chen Y., Zhu X., Quan L., Wang L., *Performance analysis of a double-salient permanent-magnet double-rotor motor using electromagnetic–thermal coupling method*, IEEE Trans. Appl. Supercond., vol. 26, no. 4, pp. 1–5 (2016), DOI: 10.1109/TASC.2016.2543598.

[13] Tahavvor A.R., Shokoohi N., *Simulation of turbulent natural convection heat transfer in the horizontal annulus using artificial neural networks*, Iranian J. Sci. Technol. Trans. Mech. Eng., vol. 46, no. 4, pp. 1289–1300 (2022), DOI: 10.1007/s40997-022-00500-5.

[14] Wang H., Chen J., Jiang Y., Wang D., *Coupled Electromagnetic and Thermal Analysis of Permanent Magnet Rectifier Generator Based on LPTN*, IEEE Trans. Magn., vol. 58, no. 2, pp. 1–5 (2022), DOI: 10.1109/TMAG.2021.3085089.

[15] Ryu J.-Y., Hwang S.-W., Chin J.-W., Hwang Y.-S., Yoon S.W., Lim M.-S., *Mathematical Modeling of Fast and Accurate Coupled Electromagnetic-Thermal Analysis*, IEEE Trans. Ind. Appl., vol. 57, no. 5, pp. 4636–4645 (2021), DOI: 10.1109/TIA.2021.3086823.

[16] Li Z., Chen Q., Wang Q., *Analysis of multi-physics coupling field of multi-degree-of-freedom permanent magnet spherical motor*, IEEE Trans. Magn., vol. 55, no. 6, pp. 1–5 (2019), DOI: 10.1109/TMAG.2019.2899259.

[17] Yu Q., He C., Tian L., Wang X., Cheng Y., *Flux linkage estimation with saliency and can effect of a can-shielded switched reluctance motor using a simple circuit network model*, Int. J. Appl. Electromagn. Mech., vol. 56, no. 1, pp. 103–113 (2017), DOI: 10.3233/JAE-170109.

[18] Wang J., Cheng M., Qin W., Liu Q., *Fast Calculation Method of Bi-Direction Coupling Between Electromagnetic-Thermal Field for FSPM Motor*, IEEE Trans. Magn., vol. 59, no. 12, pp. 1–9 (2023), DOI: 10.1109/TMAG.2023.3323566.

[19] Li H., Krein P.T., Jin J.-M., *Electromagnetic-Thermal Modeling of Nonlinear Magnetic Materials*, IEEE J. Multiscale Multiphys. Comput. Technol., vol. 8, pp. 1–10 (2023), DOI: 10.1109/JMMCT.2022.3229963.

[20] Dong B., Wang K., Han B., Zheng S., *Thermal analysis and experimental validation of a 30 kW 60000 r/min high-speed permanent magnet motor with magnetic bearings*, IEEE Access, vol. 7, pp. 92184–92192 (2019), DOI: 10.1109/ACCESS.2019.2927464.

[21] Zhao H., Zuo W., Li Q., Cheng Q., Pan N., Zhou K., *Thermal–hydraulic performance optimization of the spiral cooling channel in surface type permanent magnet synchronous motor*, J. Thermal Anal. Calorimetry, vol. 148, no. 19, pp. 10345–10355 (2023), DOI: 10.1007/s10973-023-12390-z.

[22] Hu X., Shi G., Lai Y. *et al.*, *Temperature Rise Calculation of the High Speed Magnetic Suspension Motor Based on Bidirectional Electromagnetic–Thermal–Fluid Coupling Analysis*, Machines, vol. 11, no. 3 (2023), DOI: 10.3390/machines11030364.

[23] Liu C., Li Y., Zhang H. *et al.*, *Performance analysis of permanent magnet claw pole machine based on magneto-electric-thermal coupling network method*, Electr. Eng., vol. 106, no. 3, pp. 3559–3572 (2024), DOI: 10.1007/s00202-023-02154-1.

[24] Ishikawa T., Qu H., Kasahara K., *Maximum efficiency of induction motors considering iron loss resistance*, IEEJ Trans. Elect. Electron. Eng., vol. 14, no. 9, pp. 1426–1427 (2019), DOI: 10.1002/tee.22947.

[25] Tong W., Sun L., Wu S., Hou M., Tang R., *Analytical Model and Experimental Verification of Permanent Magnet Eddy Current Loss in Permanent Magnet Machines with Nonconcentric Magnetic Poles*, IEEE Trans. Ind. Electron., vol. 69, no. 9, pp. 8815–8824 (2022), DOI: 10.1109/TIE.2021.3111573.

[26] Zehri A.H., Nylander A., Ye L., Liu J., *Graphene-coated copper nanoparticles for thermal conductivity enhancement in water-based nanofluid*, in 2019 22nd Eur. Microelectronics Packag. Conf. Exhib., Pisa, Italy, pp. 1–7 (2019), DOI: 10.23919/EMPC44848.2019.8951883.

[27] Naito T. *et al*., *Thermal conductivity of YBCO coated conductors reinforced by metal tape*, IEEE Trans. Appl. Supercond., vol. 21, no. 3, pp. 3037–3040 (2011), DOI: 10.1109/TASC.2010.2089481.

[28] Bagrets N., Heller R., Weis J.R., Weiss K.P., *Thermal resistance between metallic surfaces of copper and stainless steel at different temperatures and applied forces for high current HTS cable-in-conduit conductors*, IEEE Trans. Appl. Supercond., vol. 32, no. 6, pp. 1–5 (2022), DOI: 10.1109/TASC.2022.3154327.

[29] Shanin Y.V., Bondar A.S., Chmilenko F.V., Zhang Q., *Neural network for predicting the thermal conductivity of steel with the Bayesian method using matlab software*, in 2021 IEEE Con. Russian Young Researchers Elect. Electron. Eng. (ElConRus), St. Petersburg, Moscow, Russia, pp. 1083–1087 (2021), DOI: 10.1109/ElConRus51938.2021.9396378.